On aluminum nanoparticles as substrates for metal-enhanced fluorescence in the ultraviolet for the label-free detection of biomolecules

Mustafa H. Chowdhury[1], Krishanu Ray[1], Stephen K. Gray[2], James Pond[3], Joseph R. Lakowicz[1*]

[1] *Center for Fluorescence Spectroscopy, Medical Biotechnology Center, University of Maryland School of Medicine, 725 West Lombard Street, Baltimore, MD, 21201, USA*
[2] *Chemical Sciences and Engineering Division, Argonne National Laboratory, 9700 South Cass Avenue, Argonne, IL 60439, USA*
[3] *Lumerical Solutions Inc., 201 – 1290 Homer Street, Vancouver, BC, Canada, V6B 2Y5*

Corresponding author: lakowicz@cfs.umbi.umd.edu

Supporting Tables:

Table S-1: Computed enhancement/quenching of the total power radiated in the 300-420 nm range (integrated around a closed surface containing the Al-dipole system) by the various Al nanoparticle systems studied with the dipoles oriented perpendicular to the metal surface (P - along the *x*-axis), parallel to the metal surface (L - along *y*-axis), and orientation averaged (Z = (P+2L)/3)). The enhancement or quenching of the total power radiated indicates changes in the relative radiative decay rates of the Al-dipole system when compared to the isolated dipole. *s* is the space between the dipole and the surface of the nanoparticles for the all the systems. The diameter of the Al nanoparticles were kept constant at 80 nm. For the dimer systems, the space between the two nanoparticles is 2*s* and the dipole is located exactly midway between the Al nanoparticles.

	Perpendicular (P)	**Parallel (L)**	**Orientation Average (Z)**
Monomer, *s* = 1 nm	14.90	0.1368	5.06
Monomer, *s* = 2 nm	14.39	0.1165	4.87
Monomer, *s* = 5 nm	12.02	0.1306	4.09
Monomer, *s* = 10 nm	8.34	0.1765	2.90
Monomer, *s* = 20 nm	4.52	0.3972	1.77
Dimer, 2*s* = 2 nm	3565	0.00455	1188
Dimer, 2*s* = 4 nm	874	0.00556	291
Dimer, 2*s* = 10 nm	153	0.00631	51.02
Dimer, 2*s* = 20 nm	41.33	0.00886	13.78
Dimer, 2*s* = 40 nm	11.30	0.12437	3.84

Computational Details

The calculations were performed with the parallel FDTD option on a Dell Precision PWS690 Workstation with the following components: Dual Quad-Core Intel Xeon E5320 processors at 1.86 GHz, and 8 GB RAM. Additional post-processing of the FDTD Solutions data was performed using *MATLAB* (version 7.0) from Mathworks (Natick, MA), and OriginPro 7 from Originlab Corporation (Northampton, MA).[35] The fluorophore is modeled as a time-windowed, oscillating point source for the electric field, with frequency content spanning the spectral range (100-700 nm) of interest and polarization either perpendicular or parallel to the metal nanoparticle surface. After testing for convergence, we employed a grid size of 0.5 nm for the 20 nm metal nanoparticles, and 1 nm for the 40, 80, 100 and 140 nm metal nanoparticles. Typically the durations of our simulations were 400 fs.

We perform calculations for fluorophores near one metal nanoparticle and between two metal nanoparticles. For reference we also determine the optical spectra for the nanoparticle systems in the absence of fluorophores which are obtained by use of a time-windowed plane wave (far field) excitation. Figure S1 is a schematic illustration of the two metal nanoparticles or a dimer system where d is the diameter of each nanoparticle, $2s$ is the distance between the metal surfaces, θ is the polar angle from the z-axis where $0 \leq \theta \leq \pi$, and Φ is the azimuthal angle in the x-y plane from the x-axis with $0 \leq \Phi < 2\pi$. The fluorophore is placed at the origin so that it is a distance s from each metal surface. (The monomer calculations correspond to simply removing one of the nanoparticles in Fig. S-1). It is assumed the excitation stage of fluorescence has occurred and the fluorophore is now spontaneously emitting dipole radiation. We consider x and y dipole polarizations, where the x orientation of the dipole is perpendicular to the metal nanoparticle surface and the y orientation of the dipole is parallel to the metal nanoparticle surface. We assume a background relative dielectric constant of 1.0.
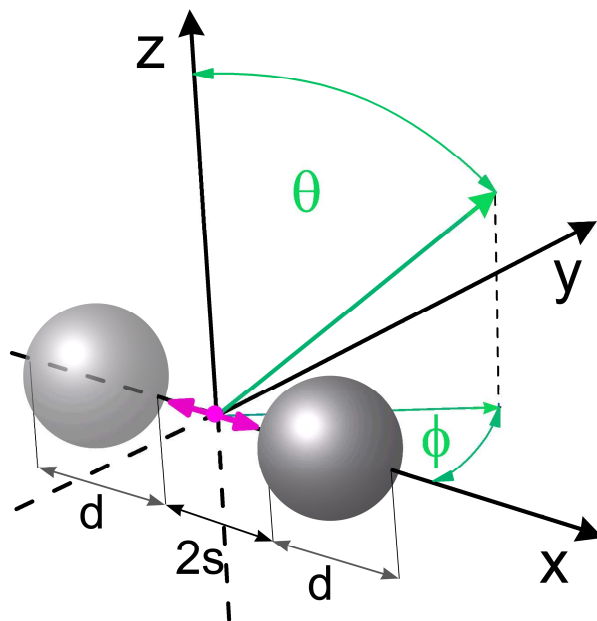
Figure S-1: Schematic diagram of a metal nanoparticle dimer/fluorophore system. The purple arrow represents the fluorophore. The fluorophores will be oriented along either the x or y axes. The single particle (monomer) systems are identical but have one of the nanoparticles removed

Experimental Details

Aluminum slugs, silicon monoxide, N-acetyl-L-tryptophanamide (NATA), and low molecular weight polyvinyl alcohol (PVA, MW 13000 - 23000) were purchased from Sigma-Aldrich and used as

received. N-acetyl-L-tyrosinamide (NATA-tyr) was obtained from Acros Organics. Distilled water (with a resistivity of 18.2 MΩ-cm) purified using Millipore Milli-Q gradient system was used for sample preparation. Aluminum was deposited on quartz slides using an Edwards Auto 306 Vacuum Evaporation chamber under high vacuum ($<5x10^{-7}$ Torr). In each case, the metal deposition step was followed by the deposition of 5 nm of silica via evaporation without breaking vacuum. This step served to protect the metal surface as well as it adds a spacer layer between the metal surface and fluorophore. The deposition rate was adjusted by the filament current and the thickness of film was measured with a quartz crystal microbalance. An aliquot of approximately 500 µl of 0.25 wt % aqueous solution of low molecular weight PVA containing separately dissolved NATA and NATA-tyr was spin coated at 3000 rpm (Specialty coating system Inc., Speedline Technologies, Indiana) on the surface of the aluminum and quartz substrates respectively. This composition of PVA forms ~15 nm thick films.

Fluorescence spectra of the amino acids on solid substrates were recorded using a Varian Cary Eclipse Fluorescence Spectrophotometer. Both the steady-state and time-domain lifetime measurements were carried out using front face illumination. Time-domain lifetime measurements were obtained on a PicoQuant lifetime fluorescence spectrophotometer (Fluotime 100). The excitation source was a pulsed laser diode (PicoQuant PDL800-B) with a 20 MHz repetition rate. The Instrument Response Function (IRF) is about 450 ps. The excitation wavelength used was 280 nm. Intensity decays were measured through bandpass interference filters. Emission lifetimes were measured with vertically polarized excitation. Magic angle observation was used in the emission path for the time-domain measurements. This optical configuration reduced the scattered light of the excitation wavelength without significant distortion of the spectra or lifetimes.

The fluorescence intensity decays were analyzed in terms of the multiexponential model as the sum of individual single exponential decays,[19]

$$I(t)=\sum_{i=1}^{n}\alpha_i \exp\left(-t/\tau_i\right)$$ Eq. (S-1)

In the above expression, τ_i are the decay times and α_i are the amplitudes and $\sum_i \alpha_i = 1.0$. The fractional contribution of each component to the steady-state intensity is described by

$$f_i = \frac{\alpha_i \tau_i}{\sum_j \alpha_j \tau_j}$$ Eq. (S-2)

the mean (intensity weighted) lifetime is represented by

$$\bar{\tau} = \sum_i f_i \tau_i$$ Eq. (S-3)

and the amplitude weighted lifetime is given by:

$$\langle\tau\rangle = \sum_i \alpha_i \tau_i$$ Eq. (S-4)

The values of α_i and τ_i were determined using the PicoQuant Fluofit 4.1 (Professional Version) software with the deconvolution of instrument response function and nonlinear least squares fitting. The goodness-of-fit criterion was determined by the χ^2 value.[19] We performed control measurements on the quartz and aluminum surfaces without either NATA or NATA-tyr that yielded almost no signal when observed through the set of band-pass emission filters used to detect the corresponding emission from those probes. This confirms that our time-domain lifetime measurements were not corrupted by the scattered incident light or emission from aluminum.

A portion of the aluminum film sample was cut and mounted on an aluminum stub with conductive tape, and then observed in an Hitachi SU-70 scanning electron microscope (SEM) directly, i.e., without any further treatment of the sample. Due to the nonconductive substrate (quartz), ultra-low voltage was employed for high resolution shallow surface observation and imaging using beam

deceleration technology. Samples were surveyed at low magnifications to see the general features and the homogeneity. Representative areas were selected for higher magnification investigation.

Supporting Results and Discussion

In the case d = 40 nm aluminum nanoparticles, the main extinction peak is red-shifted relative to d = 20 nm and occurs at $\approx$ 170 nm [Fig. S-2(a)]. Interestingly, we observe the emergence of a higher order (quadrupolar) mode at $\approx$ 133 nm. The extinction for this particle size is beginning to be dominated by the scattering component, although there is still a significant absorptive component. Similar to d = 20 nm aluminum nanoparticles, the extinction cross sections are several times larger than the physical cross section. The radiated power enhancements for fluorophores oriented perpendicular to the metal surface are shown in Fig. S-2(b). The enhancement for both fluorophore-metal spacings considered has features similar to the optical spectra [Fig. S-2(a)] with slight red shifts. For example, the enhancement dipolar peak in Fig. S-2(b) is at $\approx$ 180 nm and we see a quadrupolar enhancement peak at $\approx$ 137 nm. This latter peak is more pronounced for s = 5 nm than for s = 10 nm and indicates that higher order radiation modes are more likely to be important when the radiating dipole and the metal surface are in very close proximity.
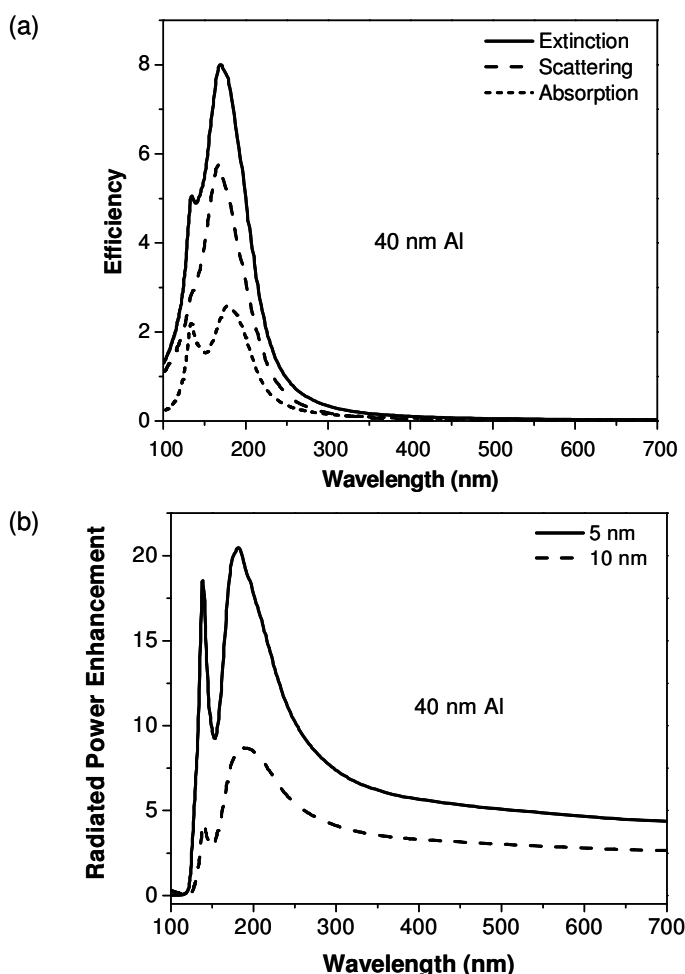
Figure S-2: (a) Extinction, scattering and absorption efficiency of a 40 nm aluminum nanoparticle; (b) Radiated power enhancement for a dipole spaced 5 and 10 nm respectively from a 40 nm aluminum nanoparticle. All the dipoles in this calculation were oriented perpendicular (along x-axis) to the surface of the Al nanoparticle.

The trends established with the d = 20 nm, 40 nm, and 80 nm particles continue with the d = 100 nm aluminum nanoparticle (Fig. S-3). The dipolar mode in the optical spectra has further red-shifted to

≈ 300 nm and broadened, with scattering becoming still more dominant over absorption. Higher order modes are prominent in the shorter wavelength regions. The radiated power enhancement (*x*-axis or perpendicular orientation) parallels the optical cross sections with peaks that are red-shifted with respect to their optical counterparts. The closer fluorophore spacing (*s* = 5 nm) displays greater enhancement and sharper features for the higher-order modes.
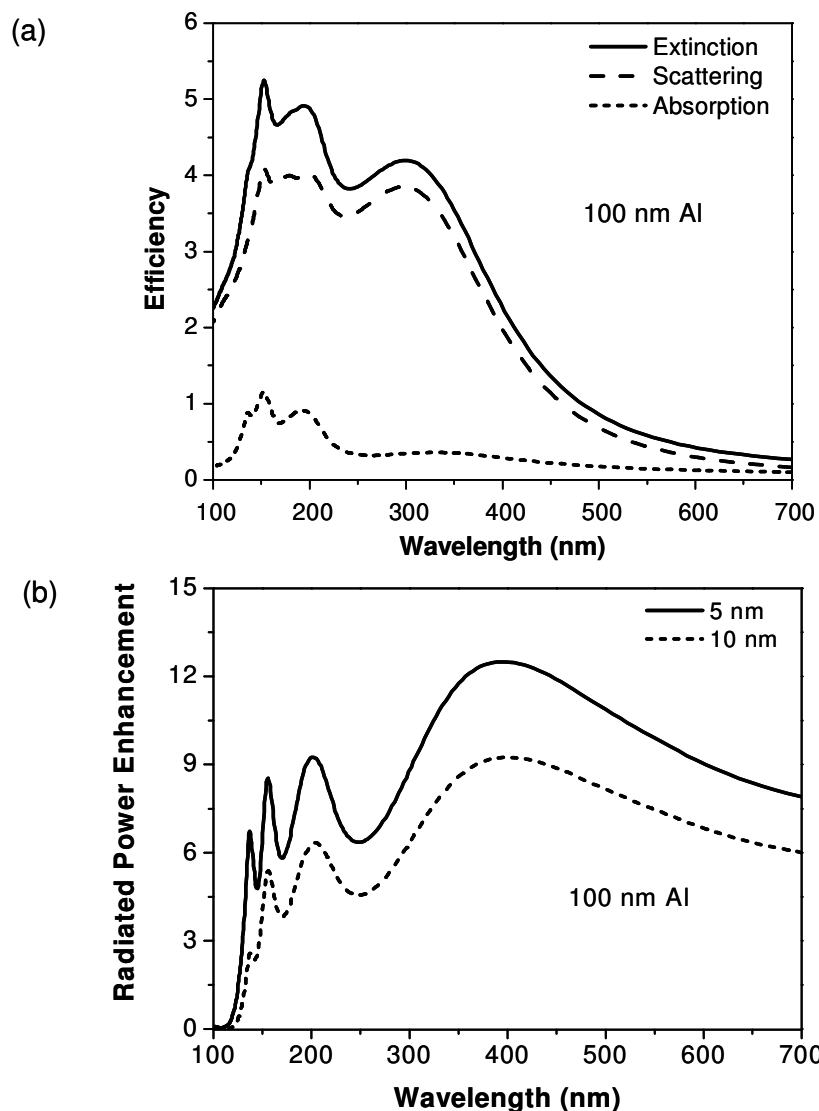
Figure S-3: (a) Extinction, scattering and absorption efficiency of a 100 nm aluminum nanoparticle; (b) Radiated power enhancement for a dipole spaced 5 and 10 nm respectively from a 100 nm aluminum nanoparticle. All the dipoles in this calculation were oriented perpendicular (along *x*-axis) to the surface of the Al nanoparticle.

Figure S-4 (a-c) compares the normalized extinction spectra and the normalized radiated power enhancement spectra for the 40 nm, 80 nm, and 100 nm aluminum nanoparticles respectively where the normalization of the both the spectra in each figure were done with respect to their dipolar peaks (most red-shifted peaks). For the case of the radiation power enhancement calculations, the dipoles were oriented along the *x*-axis (perpendicular to the nanoparticle surface) and located *s* = 5 nm from the

aluminum nanoparticles. A common theme in these figures is that the wavelength of maximum radiation enhancement for the aluminum nanoparticles is always red-shifted compared to their respective extinction peak wavelength locations. This feature is more clearly portrayed in Figure S-4 (d) where we plotted only the locations of the dipolar peaks of the radiation enhancement and the dipolar extinction peaks for the 20 nm, 40 nm, 80 nm and 100 nm aluminum nanoparticles. An interesting observation in Figure S-4 (d) is that the degree of the red-shifting of the radiation enhancement peak compared to the extinction peak increases with particle size.
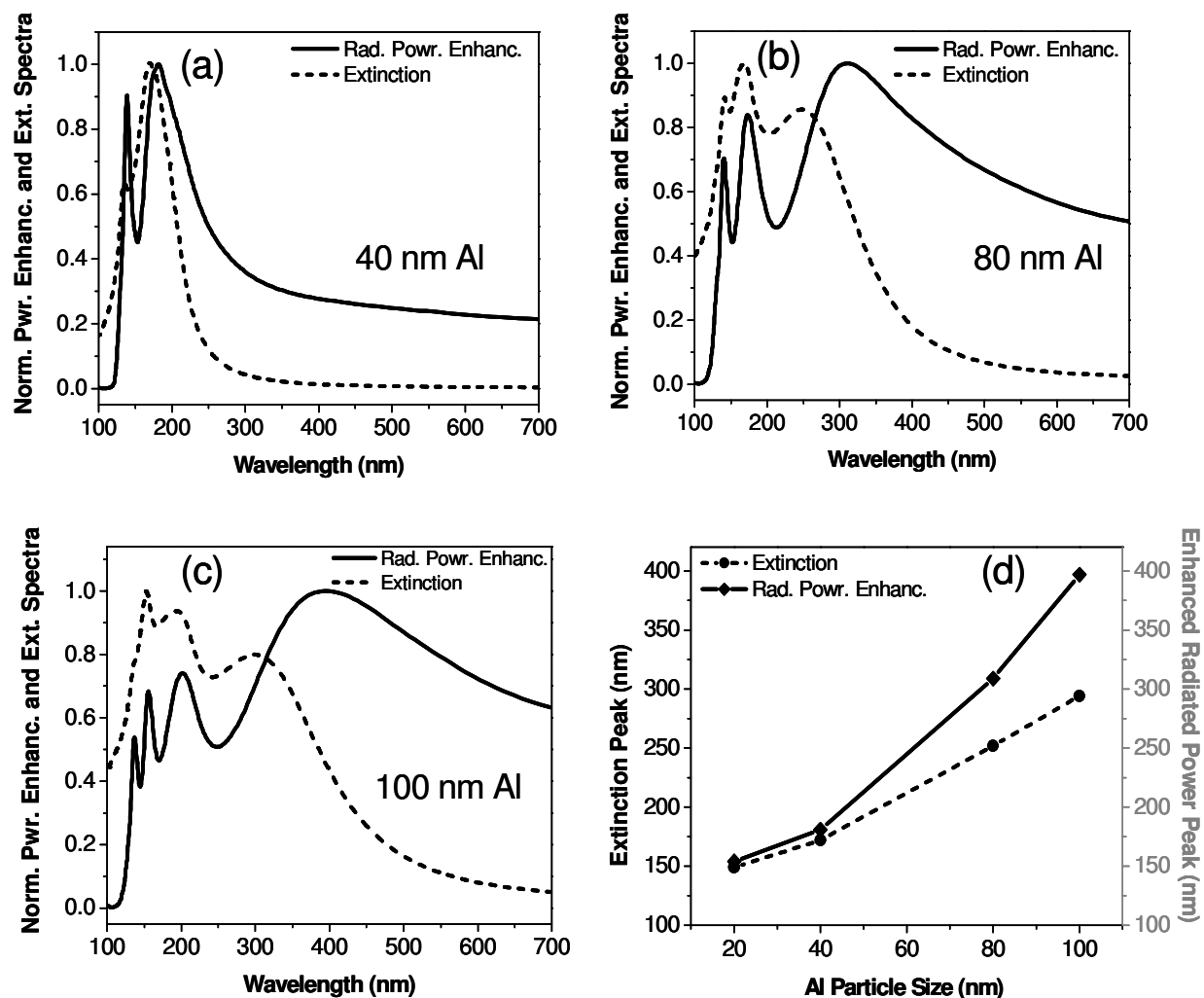
Figure S-4: Normalized extinction spectra and nomalized radiated power enhancement spectra for a dipole spaced 5 nm respectively from: (a) 40 nm; (b) 80 nm; (c) 100 nm aluminum nanoparticle - the normalization of the extinction spectra and the radiated power enhancement spectra are done with respect to their dipolar peaks (most red-shifted peaks); (d) plot of the relationship between the location of dipolar peaks of the extinction and radiated power enhancement spectra for all the aluminum particle sizes studied.

Figure S-5 (a-d) shows the comparison of the wavelength dependent radiated power enhancement for a dipole spaced $s = 5$ nm from $d = 20$ nm, 40 nm, 80 nm and 100 nm aluminum and silver nanoparticles respectively. All the dipoles in these calculations were oriented perpendicular (along x-axis) to the surface of the metal nanoparticle. In these figures we see that for wavelengths between 300-350 nm (which is primarily the emission region for the amino acids tryptophan and tyrosine in

proteins, and all the DNA bases), the aluminum nanoparticles generate larger radiated power enhancements than the silver. These results indicate that for this wavelength range, aluminum can serve as a better substrate than silver for creating MEF. This conclusion is one of the main motivations for studying the feasibility of using aluminum as MEF substrates for the label free detection of biomolecules in the UV range. However, for $\lambda > 380$ nm, silver nanoparticles begin to show greater radiated power enhancements than aluminum. Since protein emission spectra are broad with tail that extend well past $\lambda \sim 380$ nm, Figure S-5 indicates that silver can potentially still be used as a reasonable MEF substrate.
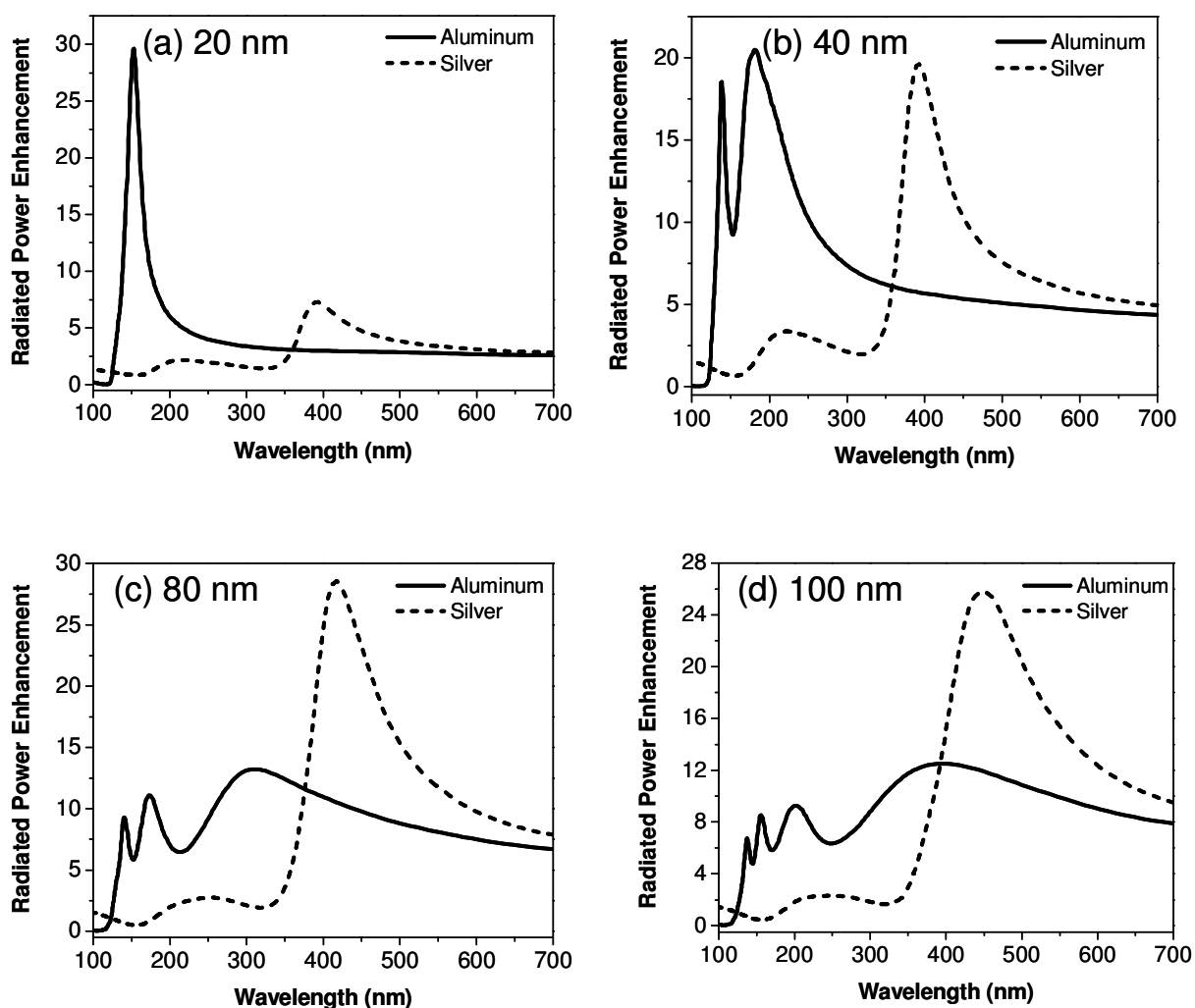
Figure S-5: Comparison of the radiated power enhancement for a dipole spaced 5 nm from (a) 20 nm; (b) 40 nm; (c) 80 nm; (d) 100 nm aluminum and silver nanoparticles respectively. All the dipoles in these calculations were oriented perpendicular (along *x*-axis) to the surface of the metal nanoparticles.
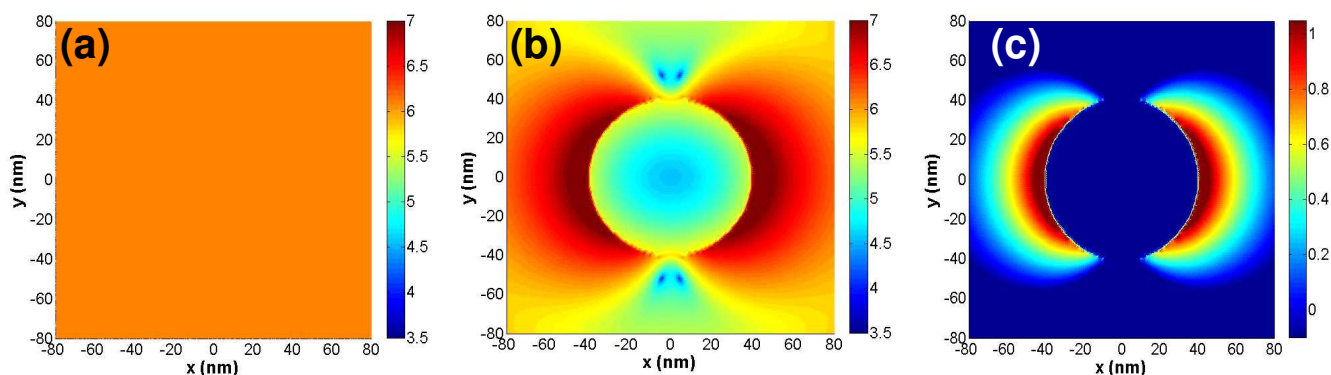
Figure S-6 (a) shows the near-field intensity image of a plane wave of wavelength 280 nm with its electric field oriented along the *x*-axis and its propagation vector along the *z*-axis (out of the plane of paper). Since we are observing the plane wave along its planar wavefront, we see an image of uniform intensity. Figure S-6 (b) shows the near-field intensity image of the fields created around an 80 nm aluminum nanoparticle by its interaction with the plane wave of Figure S-6 (a). Figure S-6 (c) shows the image of the near-field enhancements around the 80 nm aluminum nanoparticle by its interaction with

the plane wave of Figure S-6 (a). This image is generated by dividing the raw data of Fig. S-6 (b) by the data of Fig. S-6 (a). Note all images are in the log scale (base 10). Figure S-6 (c) clearly reveals that the interaction of aluminum nanoparticles with 280 nm incident light produces regions of high field enhancements around the nanoparticle. The field intensity patterns in these regions show an enhancement of over 10-fold in some areas. Hence a protein molecule immobilized to the aluminum particle in this region will experience a much higher excitation field than if it were isolated and directly excited only by the incident light. This will lead to higher excitation rates of the fluorophore, which leads to greater excitation-emission cycles in a given time period. The enhanced radiation power calculations presented in Figures 1-2 and S-2, S-3 signifies an increase in the radiative decay rate of the fluorophore when it is next to the aluminum particle. This increase in the radiative decay rate can also potentially decrease the excited state lifetime of the fluorophore (providing the non-radiative decay pathways are not enhanced by the aluminum). Thus a shorter excited-state lifetime combined with an increased excitation-emission cycle can translate to an increase in the number of photons emitted by the fluorophore in a given time period (providing the excited-state molecule is not saturated).


Figure S-6: (a) Near-field intensity image of a plane wave of wavelength 280 nm oriented along the *x*-axis and propagating along the *z*-axis (out of the plane of paper); (b): Near-field intensity image of the fields created around an 80 nm aluminum nanoparticle by its interaction with the plane wave of Figure 11 (a); (c): Near-field image of the field enhancement around an 80 nm aluminum nanoparticle by its interaction with the plane wave of Figure S-6 (a). This image is generated by diving Fig. S-6 (b) by Fig. S-6 (a). Note all images are in the log scale (base 10).

Figure S-7 (a) shows the electric field intensity in the *x-y* plane around an isolated perpendicular fluorophore (dipole axis is along the *x*-axis) emitting at 350 nm. To obtain the wavelength-resolved result we keep the fluorophore or dipole oscillating at a fixed frequency corresponding to 350 nm throughout the entire simulation time and construct a time average of the square of the electric field vector over the last period of evolution. We choose 350 nm as this wavelength is the peak emission wavelength of protein fluorescence. It is interesting to note that the isolated dipole has near-fields along

both the *x* and *y* axes. We have verified, as might be expected, that the intensity of Figure 12 (a) is very similar to the near-field of a Hertz dipole. Figure S-7 (b) shows the near-fields around an 80 nm aluminum nanoparticle with the dipole located 5 nm from its surface. It is important to note that the near-fields observed in Figure S-7 (b) are not necessarily radiative and thus not indicative of the radiated power. Figure S-7 (c) is an image of the near-field enhancement and quenching that is generated by dividing the data in Figure S-7 (b) by the data in Figure S-7 (a). The images are displayed in the logarithmic scale (base 10) for clarity of presentation. The areas in Figure S-7 (c) which correspond in the color map to negative values are areas where we see quenching of the near-field around the particle, and areas which correspond to positive values are areas where we see enhancements in the near-field. The nanoparticle system studied in Figure S-7 (according to Table S-1) shows an approximately S-7-fold enhancement in the radiated power (increase in radiative decay rate) when compared to the isolated fluorophore. The near-fields around the 80 nm aluminum particle also show enhancements as seen in Figure S-7 (c). It is interesting to observe that the near-field is not enhanced *between* the particle and the dipole, but shows the largest enhancement for the far or distal side of the particle relative to the dipole (dark red colored areas). It is also interesting to observe that the regions of near-field enhancements extend tens of nanometers away from the aluminum nanoparticle.
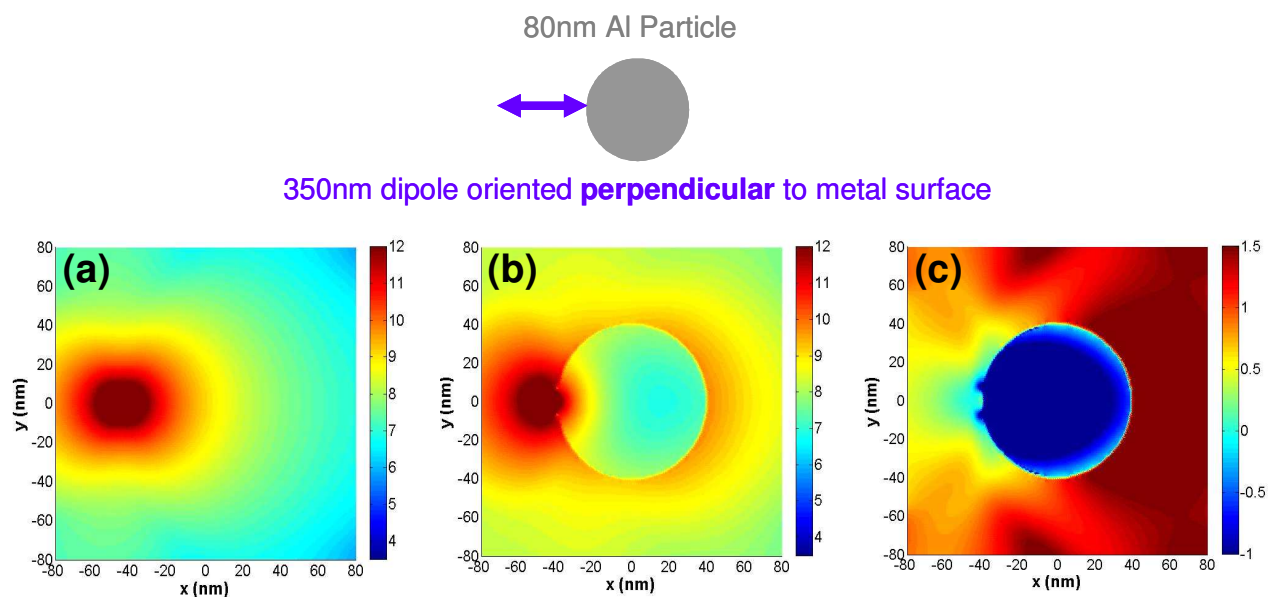

Figure S-7: Near-field intensity distribution around (a) isolated perpendicular oriented dipole (along *x*-axis) emitting at 350 nm; (b) an 80 nm aluminum nanoparticle with the dipole located 5 nm from its surface calculated using FDTD, and (c) near-field enhancement and quenching. This image is generated by diving Fig. S-7 (b) by Fig. S-7 (a). Note all images are displayed in the log scale.

The field emission scanning electron microscope (FE-SEM) image of a 10 nm thick aluminum film, the chemical structures of NATA and NATA-tyr and the schematic of the experimental system studied are shown in Figure S-8 (a-c). The SEM image reveals that the aluminum forms nanoparticles of various shapes and sizes when evaporated on the quartz substrate, with an average particle size of approximately 80 nm (a rough estimate). We selected a neutral tryptophan derivative N-acetyl-L-tryptophanamide (NATA) and a neutral tyrosine derivative N-acetyl-L-tyrosineamide (NATA-tyr) to avoid electrostatic interactions or binding of a free amino group to the metal. NATA provides essentially the same chemical structure as a tryptophan residue in protein because the amino and carboxyl groups in NATA are unchanged peptide bonds. The same holds true for NATA-tyr.

(a)

(b)

NATA   NATA-tyr

(c)
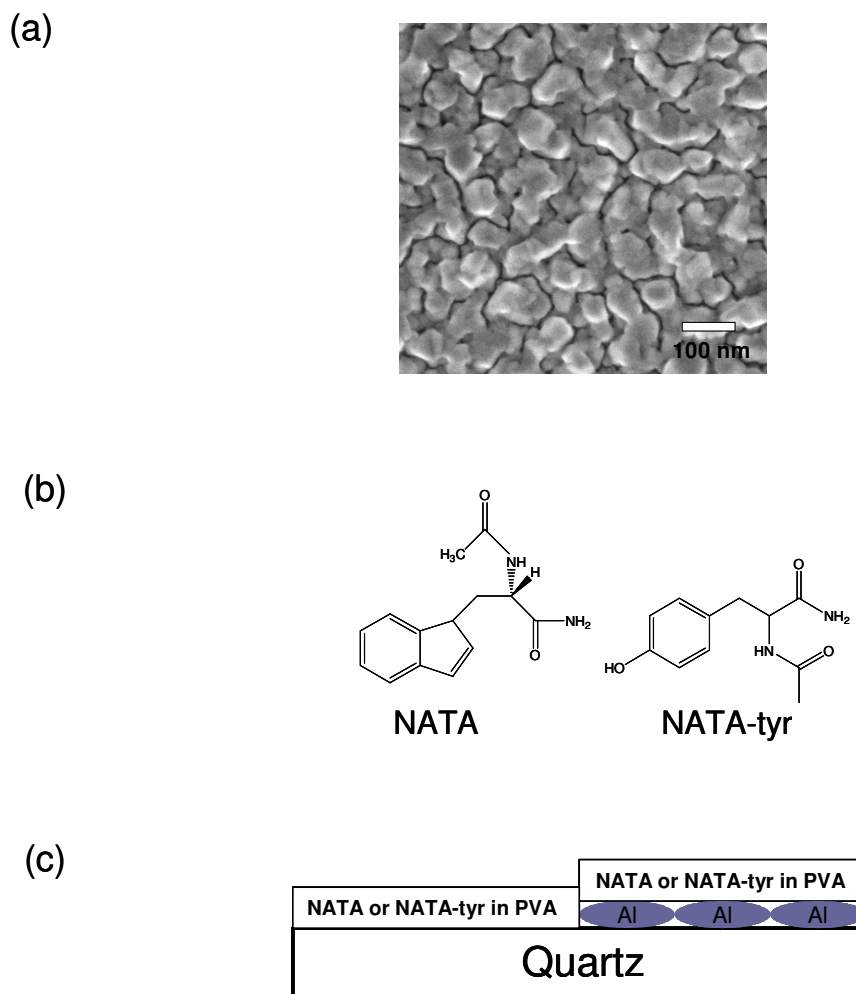
Figure S-8: (a) FE-SEM image of a 10 nm thick aluminum film on a quartz substrate; (b) Chemical structures of N-acetyl-L-tryptophanamide (NATA) and N-acetyl-L-tyrosinamide (NATA-tyr); (c) Schematic of the sample geometry.

Figure S-9 shows the photostability of NATA on quartz and aluminum substrates. Using the same incident excitation power, we observed significantly more fluorescence of from the aluminum nanostructured substrates as compared to the quartz control sample (data not shown). In Figure S-9, the incident excitation power on the aluminum was attenuated to give the similar initial emission intensity as observed on the quartz substrate. It is clearly seen in Figure S-9 that NATA is more photostable on the aluminum substrate when compared to the quartz substrate when the incident excitation yields similar emission intensities. This result is consistent with an increase in the radiative decay rate and the decrease of lifetime of NATA in the presence of aluminum nanostrucutres. Our results confirm that an increase in emission intensity coupled with a decrease in lifetime of the NATA emission on quartz causes a significant increase in its photostability, which in turn is expected to increase its detectability as the excited state molecule is able to go through a larger number of excitation-emission cycles in a given period of time without photobleaching.
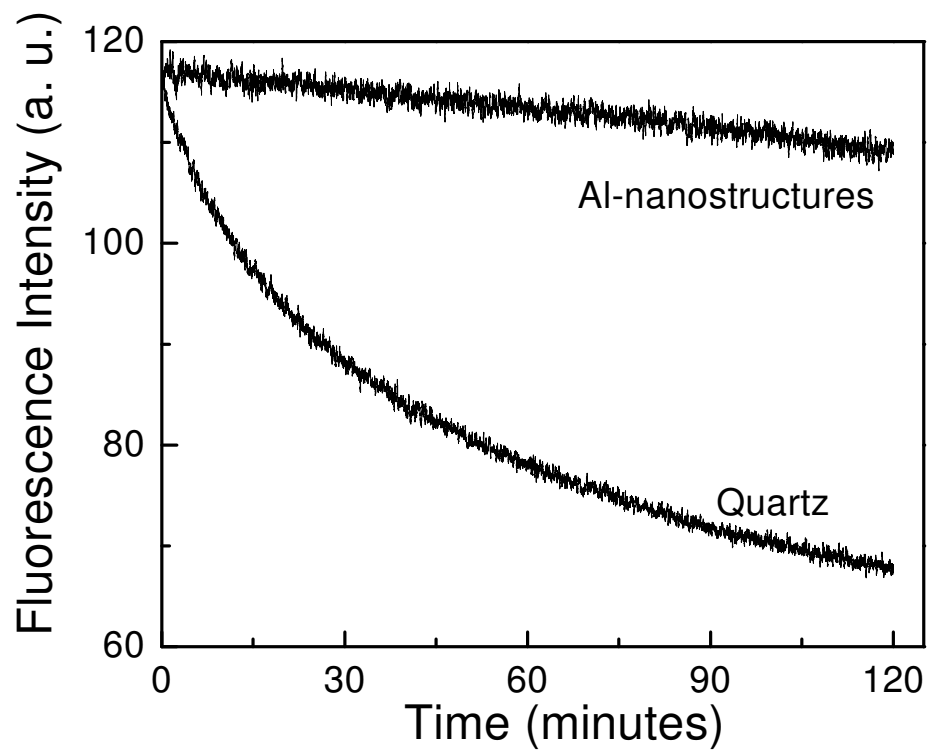
Figure S-9: Photostability of NATA on quartz and aluminum substrates.